

**FORSCHUNGSZENTRUM KARLSRUHE**

Technik und Umwelt

Wissenschaftliche Berichte

**FZKA 6058**

# **Fracture toughness and R-curve behaviour of PZT**

**T. Fett, D. Munz, G. Thun**

Institut für Materialforschung

Forschungszentrum Karlsruhe GmbH, Karlsruhe

1998

## **Fracture toughness and R-curve behaviour of PZT**

### **Abstract:**

The failure of ceramic materials is governed by the fracture toughness  $K_{Ic}$  and in case of a material with a rising crack resistance by the so-called R-curve. In this report the fracture mechanical properties of commercial PZT-ceramics are determined. Controlled fracture tests with single-edge-notched bending bars were performed in an extremely rigid loading device. The fracture toughness was determined from the maximum load and the R-curve was evaluated via the compliance method. Indirect results of  $K_{Ic}$  using the Indentation Strength (IS) method are reported.

As practical applications of the fracture mechanics data the influence of the R-curve on strength and on lifetimes in static bending tests is discussed.

## **Rißzähigkeit und Rißwiderstandskurve von PZT-Keramiken**

### **Kurzfassung:**

Das Versagen von Keramiken wird durch die Rißzähigkeit  $K_{Ic}$  und im Falle eines Materials mit ansteigendem Rißwiderstand durch die R-Kurve bestimmt. Im vorliegenden Bericht werden die bruchmechanischen Eigenschaften von kommerziellen PZT-Keramiken bestimmt. An einseitig gekerbten Biegestäben werden mit einer extrem steifen Apparatur kontrollierte Bruchversuche durchgeführt und die Rißzähigkeit aus dem Kraftmaximum und die R-Kurve über die Compliance-Methode bestimmt. Indirekte Messungen der Rißzähigkeit erfolgen mit der "Indentation Strength" Methode.

Als praktische Anwendung der erhaltenen Ergebnisse wird der Einfluß der R-Kurve auf die Festigkeit und die Lebensdauer in statischen Versuchen diskutiert.

# Contents

1 Introduction	1
2 Experiments	2
2.1 Materials investigated	2
2.2 Knoop-damaged specimens	2
2.3 Edge notched specimens	5
2.3.1 Specimen preparation, testing and evaluation procedure	5
2.3.2 Results	7
2.4 Comparison of R-curves	9
2.5 Fit relations	10
2.6 Indentation Strength method	11
3 Effect of an R-curve on tensile and bending strength	14
3.1 Stress distribution in a bending bar	14
3.2 Fracture mechanical considerations	16
3.2.1 Differences in bending and tensile strength without an R-curve	17
3.2.2 Differences in bending and tensile strength including the R-curve	18
3.3 Prediction of tensile strength from bending strength results	22
3.4 Prediction of bending strength from tensile strength results	26
4 Influence of the R-curve on lifetimes in static tests	28
5 References	31

# 1 Introduction

Failure of ceramic materials often starts from cracks, which may originate at pores and inclusions or may be generated during surface treatment. Various failure modes are responsible for failure and finite lifetimes of ceramic materials. At moderate temperatures the most important of them are:

- spontaneous failure,
- subcritical crack growth under static load,
- cyclic fatigue,
- thermal shock and thermal fatigue.

*Spontaneous failure* occurs when the applied stress reaches the strength of the material or, in terms of fracture mechanics, when the stress intensity factor  $K_I$  of the most severe crack in a component reaches or exceeds the fracture toughness  $K_{Ic}$ . Therefore,  $K_{Ic}$  must be known for the spontaneous failure behaviour to be assessed.

The loading quantity in linear-elastic fracture mechanics which governs failure is the stress intensity factor  $K$ .

The stress intensity factor  $K_I$  which is called the "mode-I" stress intensity factor and is caused predominantly by stresses normal to the crack area is of greatest importance to the strength- and failure behaviour. The stresses at a crack tip are directly related to  $K_I$  by the Sneddon equations, which are reported in most fracture-mechanics handbooks.

Failure of a component occurs when the stress intensity factor of the most severe crack reaches a critical value  $K_{Ic}$ , the fracture toughness of the material. In case of ideally brittle materials the fracture toughness is independent of the crack extension and, consequently, identical with the stress intensity factor  $K_{I0}$  necessary for the onset of stable crack growth. Early investigations on the determination of fracture toughness for piezoelectric materials have been reported by Freiman et al.[1-3]. It is a well-known fact that failure of several ceramics is influenced by an increasing crack-growth resistance curve. This is also the case for piezoelectric ceramics [4-6].

For piezoelectric ceramics the crack growth resistance behavior is substantially more complex than for usual monolithic ceramics. In the polarized state and especially in the case of an externally applied electrical field the R-curve is affected via the electrical-mechanical coupling. In this report the material behavior of piezoelectric materials is regarded exclusively in the absence of an external electrical field.

## 2 Experiments

### 2.1 Materials investigated

Fracture mechanics tests were carried out with commercial PZT-ceramics (manufacturer: PI Ceramic, Lederhose, Germany). The materials are characterised by the manufacturer as shown in Table 1.

	PIC 141	PIC 151	PIC 155
density (g/cm <sup>3</sup> )	7.80	7.80	7.70
Curie temperature (°C)	275	250	320
d <sub>31</sub> (m/V)	-115·10 <sup>-12</sup>	-170·10 <sup>-12</sup>	-140·10 <sup>-12</sup>
d <sub>33</sub> (m/V)	330·10 <sup>-12</sup>	450·10 <sup>-12</sup>	310·10 <sup>-12</sup>
S <sub>11</sub> <sup>E</sup> (10 <sup>-12</sup> m <sup>2</sup> /N)	12.6	15.0	13.2
S <sub>33</sub> <sup>E</sup> (10 <sup>-12</sup> m <sup>2</sup> /N)	13.0	11.6	18.7

**Table 1** Investigated commercial PZT-ceramics.

For the material PIC 151 the Young's modulus was determined with fast tensile tests as  $E \cong 65$  GPa in the unpoled and  $E \cong 57$  GPa in the poled modification [7][8] with the poling direction perpendicular to the specimen length axis.

### 2.2 Knoop-damaged specimens

Rectangular specimens 3x4x45 mm<sup>3</sup> made of material PIC 151 were damaged by Knoop indentations with different indentation loads  $P$ . Then the specimens were annealed above the Curie temperature at 285°C to reduce all R-curve effects (cumulated during the indentation tests) caused by domain switching ahead of the crack tip and to reduce residual stresses by the pronounced creep effects present even at room temperature. After annealing the cracks were marked with a penetration dye and could be measured easily under the optical microscope after fracturing. The initial crack depth  $a_0$  is shown in Fig.2.1a in dependence of the indentation load  $P$ . The  $a/c$ -ratio ( $c$  = half width of the crack) was  $a/c=0.95$  with a standard deviation of 0.08.

Strength tests with the Knoop-damaged bars were performed in 4-point bending and in tensile tests. For the tensile tests the bars were glued in brass cylinders with an epoxy resin. The

tensile load of a servo-hydraulic machine is transferred by nylon strings to the brass cylinders. Details are given in [7].

The bending tests were carried out with the Knoop cracks in the tensile region. The elastically calculated bending strength data are represented in Fig.2.1b by the open circles and the tensile strength data by the solid circles.

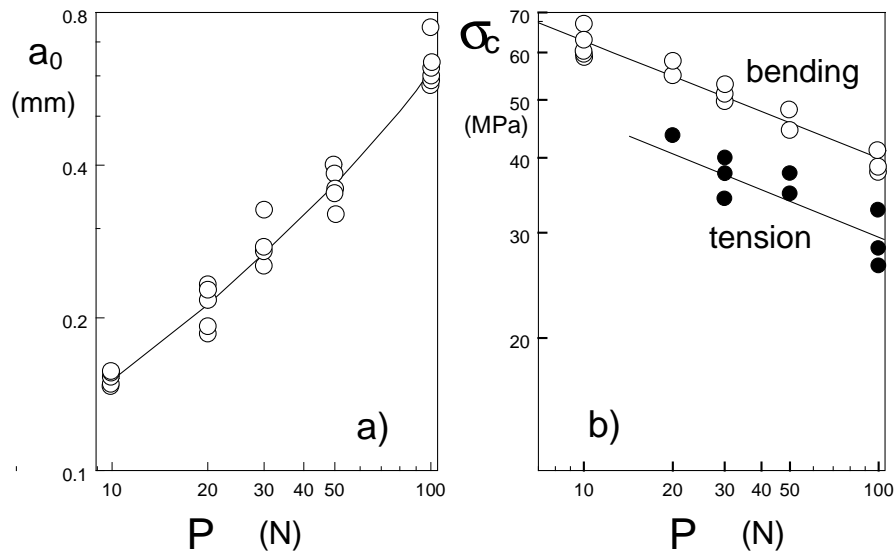


**Fig.2.1** Strength tests with Knoop-damaged specimens, a) initial crack depth  $a_0$  as a function of the indentation load, b) elastically calculated bending strength and tensile strength.

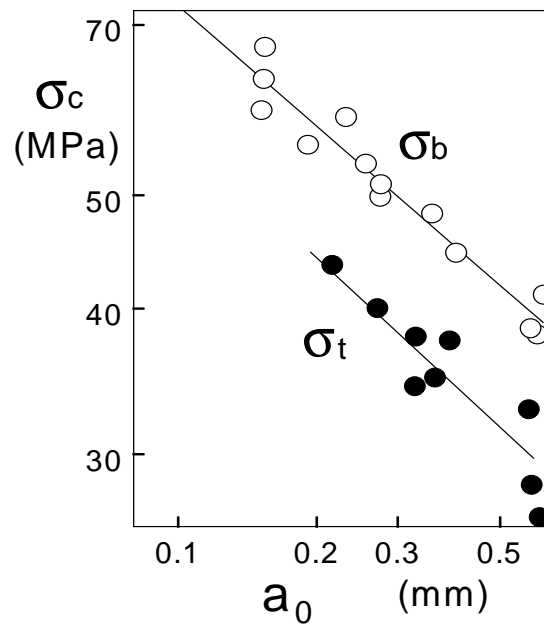


**Fig. 2.2** Bending strength  $\sigma_b$  and tensile strength  $\sigma_t$  as functions of the initial crack depth  $a_0$ .

The bending strength  $\sigma_b$  and the tensile strength  $\sigma_t$  of the indentation damaged specimens are plotted in Fig. 2.2 as functions of the initial crack size  $a_0$  in a log-log scale. The straight line behaviour of the bending strength can be expressed as

$$\sigma_b = 33. \text{MPa} a_0^{-0.34} \quad (2.1a)$$

with  $a_0$  in mm. The tensile data lead to

$$\sigma_b = 24.5 \text{MPa} a_0^{-0.37} \quad (2.1b)$$

The significant deviations from straight lines with exponents  $-1/2$  are first indications for a R-curve effect in the investigated PZT-material.

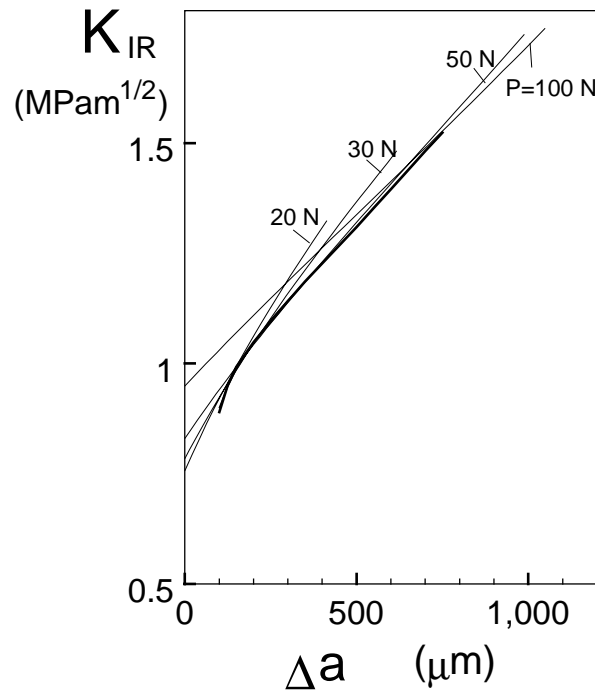


**Fig.2.3** R-curve, determined from the tangent condition for Knoop indentation cracks of different size (different indentation loads). Computations performed with constant aspect ratio ( $a/c=1$ ).

For an auxiliary stress intensity factor  $K^*$ , formally computed with the initial crack dimensions and the maximum stress (i.e. the strength)

$$K^* = \sigma_c \sqrt{\pi a_0} F(a_0 / W) , \quad (2.2)$$

it must hold

$$K_{I0} \leq K^* \quad (2.3)$$

since the maximum stress  $\sigma_c$  is larger than the actual stress at the onset of crack extension. Equation (2.2) enables to provide an upper limit of  $K_{I0}$ . From the tensile strength data of Fig. 2.1b and the related crack sizes of Fig. 2.1a it results with the geometric function  $F(a_0/W)$  for bending (proposed by Newman and Raju [9]):  $K_{I0} \leq 0.73 \text{ MPa m}^{1/2}$ .

The tensile strength results of Fig. 2.1b enable to estimate the shape of the R-curve. Since in a load-controlled test the tangent condition (see eqs.(3.4a) and (3.4b)) is fulfilled at failure, the stress intensity factors computed with the strength as the critical stress  $\sigma = \sigma_c$  must provide an envelope for the R-curve. For a first rough computation let us assume the aspect ratio of the extending cracks to remain constant ( $a/c = a_0/c_0 = \text{const.}$ ).

The curves  $K=f(\sigma_c, \Delta a)$  are entered in Fig. 2.3 as thin lines (with the Knoop indentation load as the parameter, standing for the initial crack size). The R-curve resulting from the envelope condition is introduced as thick line. A strong increase of  $K_{IR}$  with crack extension  $\Delta a$  is obvious.

## 2.3 Edge notched specimens

### 2.3.1 Specimen preparation, testing device and evaluation procedure

In rectangular bars with dimensions 3x4x45 mm narrow notches with very small notch root radii were introduced using the razor blade method as proposed by Nishida et al. [10]. Stable crack extension tests were performed with single edge notched specimens.

For the controlled fracture tests it is necessary to apply a test arrangement with a low compliance. In order to perform such tests with extremely rigid testing device the three-point bending arrangement shown in Fig. 2.4 was used.

A specimen with depth  $W = 4 \text{ mm}$  is loaded with an externally applied increasing load. The effective load - acting on the specimen - is measured with a quartz load cell, and the displacement is recorded by an inductive displacement pick-up.

The actual crack length was determined by a combination of the linear-elastic compliance formula and an experimental correction. In the first step the crack length has been evaluated by linear-elastic analysis from the compliance, neglecting the effect of the R-curve on the compliance. The total compliance  $C$  consists of the compliance of the uncracked bar  $C_0$ , the portion  $\Delta C$  caused by the crack, and a 'parasitic' compliance  $C_{par}$  summarising additional elastic settling and elastic deformation of the supporting rollers and the supporting structure

$$C = C_0 + C_{par} + \Delta C \quad (2.4)$$



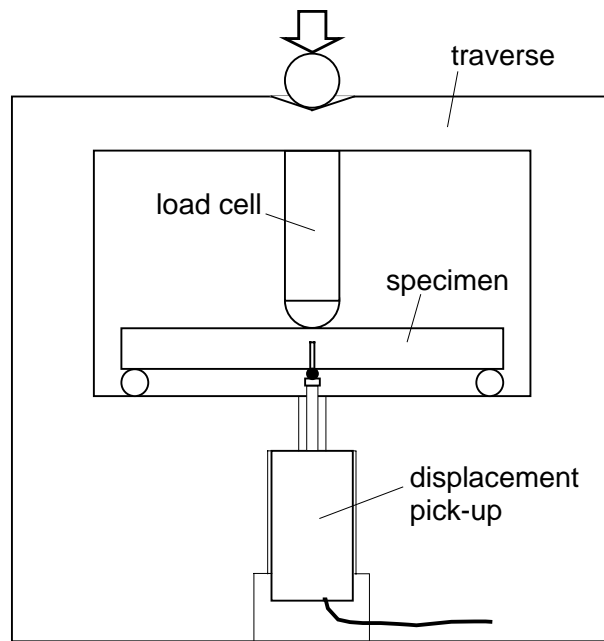


**Fig. 2.4** Testing device for stable crack growth measurements.

The compliance part due to the crack ( $\Delta C$ ) can be obtained for any ratio  $W/L \geq 2$  ( $L$  = supporting roller span) from [11]. Several tests were suspended after a certain amount of crack growth (prior final fracture) and the cracks were infiltrated with a penetration dye. After drying the specimens were fractured and the real crack length was measured under an optical microscope. In Fig. 2.5 the crack length obtained with the compliance method  $a_{\text{comp}}$  is plotted versus the physical crack length  $a_{\text{opt}}$ . For small amounts of crack extension ( $\Delta a < 0.5$  mm) the deviations between the two types of crack length were found to be negligible. For larger  $\Delta a$  the crack length from compliance is significantly smaller than the real physical crack. Figure shows the dependency between the two crack lengths.

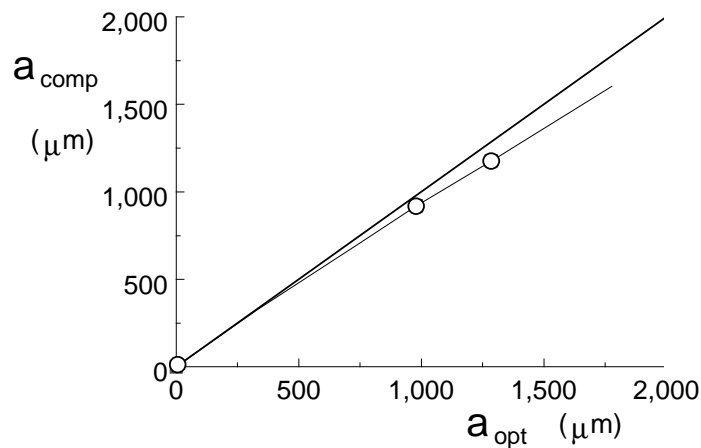


**Fig. 2.5** Comparison of crack lengths from optical evaluation and compliance measurements.

Figure 2.6 shows a typical load vs. displacement plot. The optical crack length evaluation via the compliance together with Fig. 2.5 enables to determine the correct crack length from the load versus displacement curve. From the load  $P$  recorded with the quartz load cell and the crack length  $a$  the related stress intensity factors  $K$  were computed as

$$K = \sigma_0 Y\left(\frac{a}{W}, \frac{L}{W}\right) \sqrt{a} \quad , \quad \sigma_0 = \frac{3PL}{2W^2B} \quad (2.5)$$

with the geometric function  $Y$  proposed for any  $L/W > 2$  in [11].

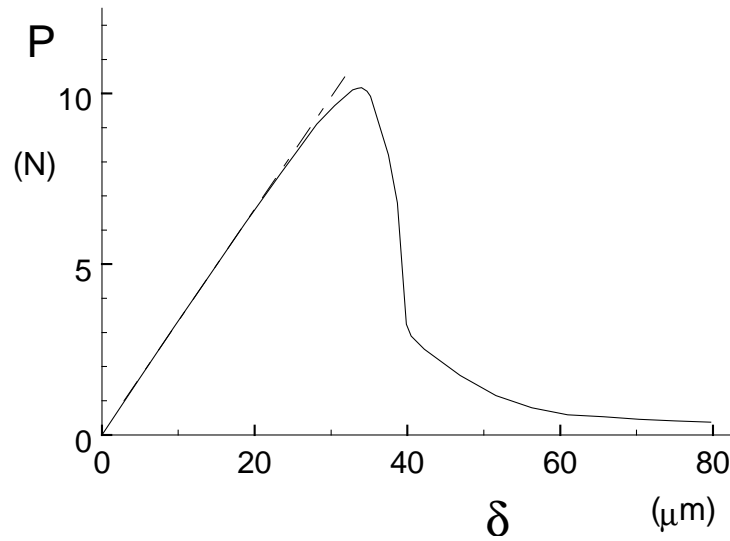


**Fig. 2.6** Load vs. displacement record for a specimen with initial notch depth  $a_0 = 1.6$  mm

### 2.3.2 Results

Two R-curves obtained for poled PIC 151 (poling direction perpendicular to the specimen length axis) are shown in Fig. 2.7 (symbols). In addition the stress intensity factors computed with the maximum load occurring in the controlled fracture test  $\sigma_{\max}$  are entered as curves. In a load-controlled fracture test failure would occur at that crack extension  $\Delta a$  at which the R-curve (symbols) and the curve  $K(\sigma_{\max})$  coincide. This is the case in Fig.2.7 for  $\Delta a \cong 300 \mu\text{m}$ . In terms of Fig. 2.6 this condition is identical with the horizontal tangent  $dP/d\delta=0$ , i.e.  $P = P_{\max}$ ,  $\sigma = \sigma_{\max}$ . The stress intensity factor for this condition is  $K_{Ic}$ , the stress intensity factor at the point of instability.

Fracture toughness data obtained in controlled fracture tests are compiled in Table 2 as average values of at least 6 specimens. The second value in each column is the standard deviation. In case of relatively deep notches ( $a_0 > 1.2\text{mm}$ ) in all cases stable crack extension with a "round maximum" (see Fig. 2.6) was found. For  $a_0 < 1.3$  mm also load-displacement

curves were observed in which only a small crack extension occurred before failure and the "round" maximum condition was not reached. The related data are marked by (\*) of Table 2.

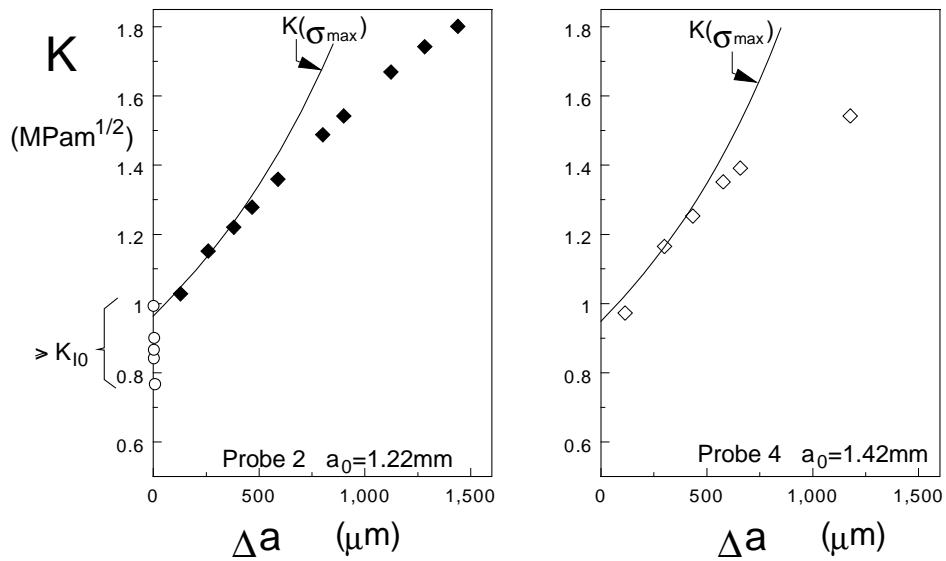


**Fig. 2.7** R-curve data for two specimens of poled PIC 151 (symbols). Curve: Stress intensity factor computed for different crack length with maximum stress occurring in the controlled fracture tests ( $\sigma = \sigma_{max}$ ).

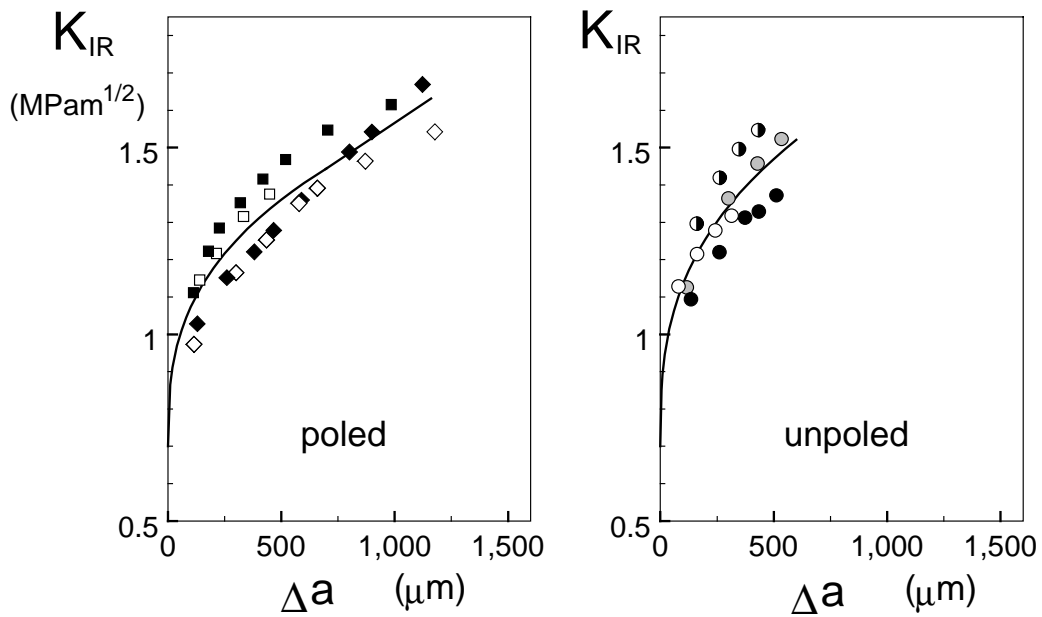


**Fig. 2.8** R-curves for poled and unpoled PZT (PIC 151) determined in controlled fracture tests with edge-notched bending bars; different symbols for different specimens.

Figure 2.8 shows R-curves for the poled and for the unpoled material. The R-curve for the unpoled material is slightly higher than the poled ceramic. The differences are about 5%, i.e. in the order of the scatter of different specimens.

	unpoled	poled
PIC 141	1.13 0.07	1.10 0.10
PIC 151	1.35 0.09	1.20 0.06
	1.17 0.045 (*)	
PIC 155	1.25 0.04	1.16 0.06

**Table 2** Fracture toughness computed from the maximum load and the related actual crack length  $a_{\max}$ . First number: Mean value, second number: Standard deviation (toughness data in  $\text{MPa m}^{1/2}$ ). (\*): notch depth  $< 1.3 \text{ mm}$  ( $\Rightarrow \Delta a \cong 0$ ).

## 2.4 Comparison of R-curves

In Fig. 2.9 the R-curve obtained in controlled fracture tests is compared with the estimation resulting from the tensile strength data of Knoop-damaged specimens. The estimated results are about 20% less than the results from edge-notched bending bars.

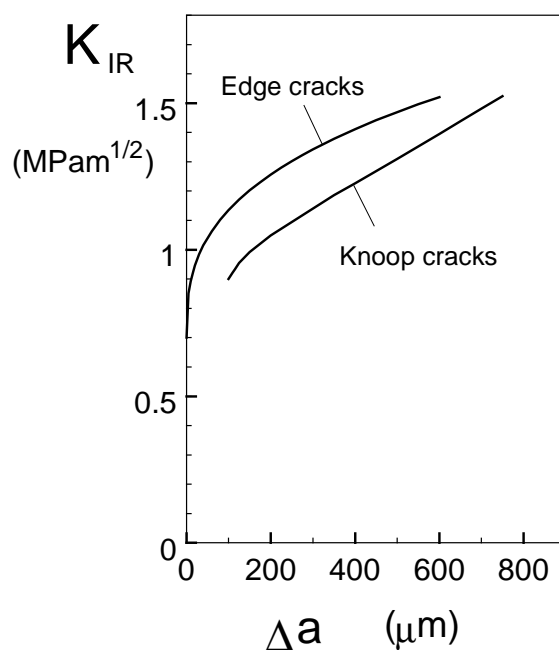


**Fig. 2.9** Comparison of R-curves obtained with edge-notched bending bars and specimens with Knoop indentation cracks.

As can be concluded from the comparison given in Fig. 2.9 the evaluation of the R-curve with Knoop-indentation cracks, assuming  $a/c = 0.95$  remaining constant during the stable crack extension, provides only a rough estimation of the real R-curve. The fact that the aspect ratio  $a/c$  changes during crack propagation becomes obvious in Section 3.2.2 (see Fig. 3.6).

## 2.5 Fit relations

A fit relation for the R-curve ( $\Delta a \leq 750 \mu\text{m}$ ) obtained with edge-cracked specimens is

$$K_{\text{IR}} = K_{\text{I0}} + A(\Delta a)^m \quad (2.6)$$

with the parameters given in Table 3.

	$K_{\text{I0}}$ (MPa $\sqrt{\text{m}}$ )	$A$ (MPa $\sqrt{\text{m}}$ )	$m$	$A'$ (MPa $\sqrt{\text{m}}$ )	$m'$
unpoled	0.7	0.085	0.354	0.521	0.164
poled	0.7	0.073	0.354	0.496	0.164

**Table 3** Parameters for a power-law description of the R-curves ( $\Delta a$  in  $\mu\text{m}$ ).

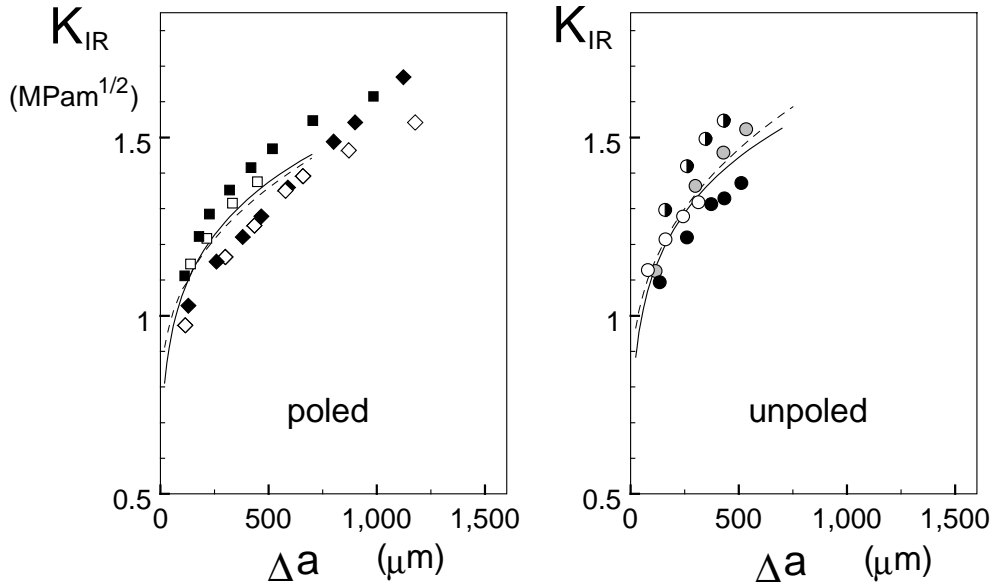


**Fig. 2.10** Fit-relations for the R-curve behaviour compared with the measured data. Solid curves: eq.(2.7), dashed curves: eq.(2.6).

For analytical computations it may be of advantage to approximate the R-curve without an initial value of  $K_{\text{I0}}$ , e.g. by

$$K_{\text{IR}} = A'(\Delta a)^{m'} \quad (2.7)$$

Table 3 contains the parameters for such an approximation. The dashed curves in Fig. 2.10 show the description with eq.(2.6), the solid curves illustrate eq.(2.7).

## 2.6 Fracture toughness determined with the Indentation Strength method

The fracture toughness  $K_{Ic}$  was determined with the indentation strength (IS) method [12]. Vickers indentations were introduced with different indentation loads and the damaged specimens were broken in 4-point bending tests. From the bending strength  $\sigma_b$ , the indentation load  $P$ , the hardness  $H$  and the young's modulus  $E$  the  $K_{Ic}$  value results as

$$K_{Ic} = 0.59 \left( \frac{E}{H} \right)^{1/8} (\sigma_b F^{1/3})^{3/4} \quad (2.8)$$

Using the Vickers-hardness  $HV = 3 \text{ GPa}$  we obtain the toughness data represented in Fig. 2.11 for PIC 151. The results can be summarised by

$$K_{Ic} = 1.45 \text{ MPa}\sqrt{\text{m}}$$

with a standard deviation of  $\cong 0.15 \text{ MPa m}^{1/2}$ . A dependency on the indentation load is negligible for PIC 141 and 151 (see Figs. 2.12 and 2.13). Therefore, mean values over all loads were determined for these two materials (see Table 4). In case of PIC 155 a significant trend of increasing IS-fracture toughness with increasing load seems to be obvious.

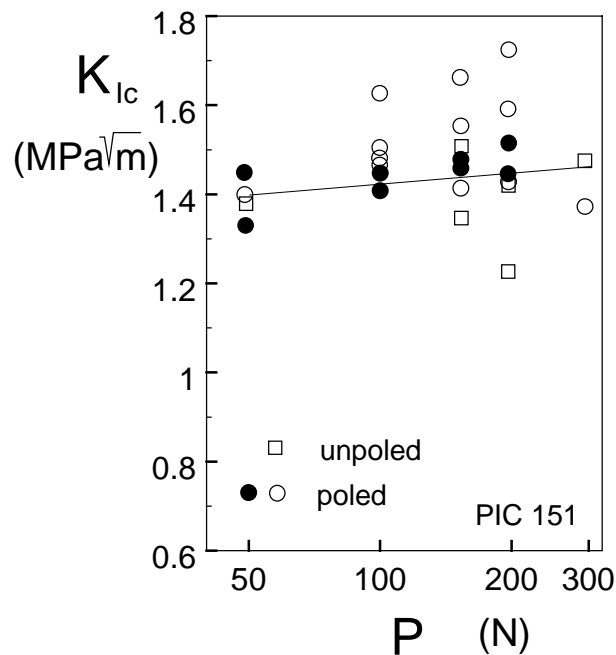


**Fig. 2.11** Fracture toughness resulting from the indentation strength method (PIC 151). Poled material: Indentation direction perpendicular to the polarisation direction (full circles), indentation load in polarisation direction (open circles).

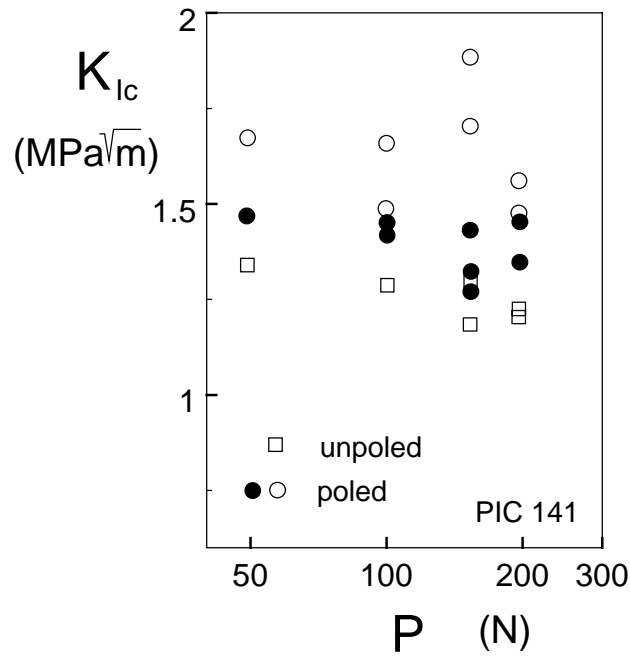


**Fig. 2.12** Fracture toughness resulting from the indentation strength method (PIC 141). Poled material: Indentation direction perpendicular to the polarisation direction (full circles), indentation load in polarisation direction (open circles).

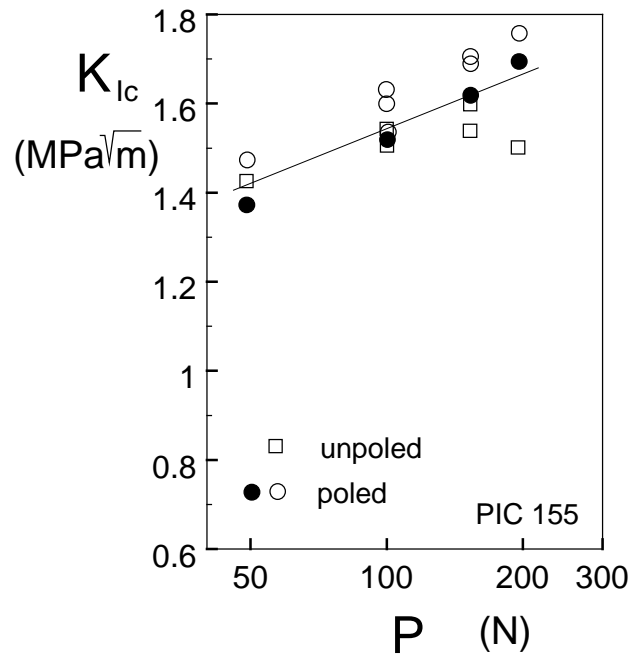


**Fig. 2.13** Fracture toughness resulting from the indentation strength method (PIC 155). Poled material: Indentation direction perpendicular to the polarisation direction (full circles), indentation load in polarisation direction (open circles).

Material	unpoled	poled (a)	poled (b)
PIC 141	1.26 MPa m <sup>1/2</sup>	1.63 MPa m <sup>1/2</sup>	batch 1), batch 2)
PIC 151	1.38 MPa m <sup>1/2</sup>	1.44 MPa m <sup>1/2</sup>	1.61 MPa m <sup>1/2</sup> , 1.45 MPa m <sup>1/2</sup>

**Table 4** Indentation strength method: (a) Indentation direction perpendicular to the polarisation direction,  
(b) Indentation direction parallel to the polarisation direction



### 3 Effect of an R-curve on tensile and bending strength

In addition to the nonlinearity of stress-strain curves electro ceramics can exhibit nonsymmetric deformation behaviour in tensile and compression tests. Tests carried out with a commercial soft PZT-ceramic showed that the plastic strains in tension exceed those under compressive stresses [7]. Nonsymmetry and nonlinearity result in complex stress distributions in non-homogeneously loaded structures. Consequently this will have consequences for the evaluation of bending tests.

#### 3.1 Stress distribution in a bending bar

A computation of the stress distribution in bending bars was performed in [7]. The resulting stresses are shown in Fig. 3.1. In Fig.3.1a the outer fibre tensile stress  $\sigma^*$ , normalised on the elastically computed bending stress  $\sigma_{el}$ ,

$$\sigma_{el} = \frac{6M}{BW^2}, \quad (3.1)$$

with the bending moment  $M$  and the specimen thickness  $B$  (here 4mm), is plotted versus  $\sigma_{el}$ . A strong stress reduction is visible. From Fig.3.1b the shape of the stress distribution can be seen. Whereas at the tensile surface the stresses are reduced, at the compressive surface the compressive stresses increase.

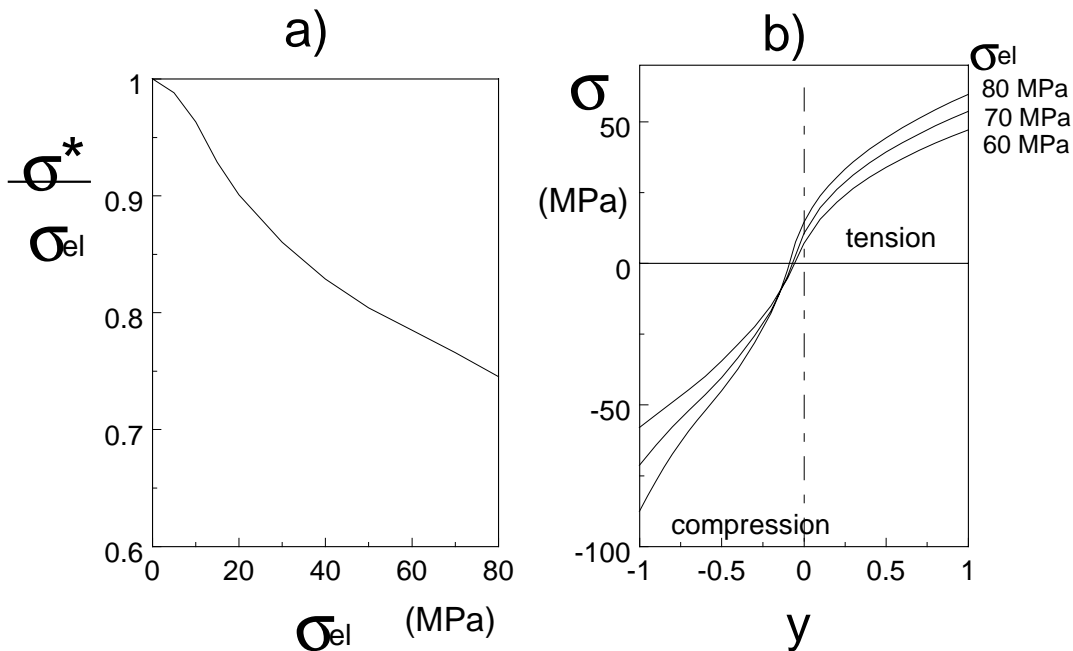


**Fig. 3.1** Stress state in a PZT bending bar as a consequence of the nonsymmetry in plastic deformation behaviour, a) Outer fibre stress  $\sigma^*$  as a function of the elastically computed bending stress  $\sigma_{el}$ , b) stress distributions for different loads.  $y=\eta/W$ ,  $\eta$ =distance from the centre line.

Figure 3.1a illustrates that e.g. for a nominal bending stress of 75MPa (the average bending strength) a real outer fibre stress of about 75% of the elastically computed stress is present. This strong stress reduction in bending is the main reason for the different strength results in tension and bending.

A rising R-curve causes differences in the strengths resulting from tension and bending tests. In order to estimate the effect of the R-curve on tensile and bending strength we consider the pure tensile case (line 1 in Fig. 3.2) and two approximations of the nonlinear stress distributions in the bending bar. An upper limit case for the stress in the tensile region is given by line (2) in Fig. 3.2, which has the correct outer fiber stress value  $\sigma^*$  and the correct stress gradient. As a lower limit case we consider straight line (3).

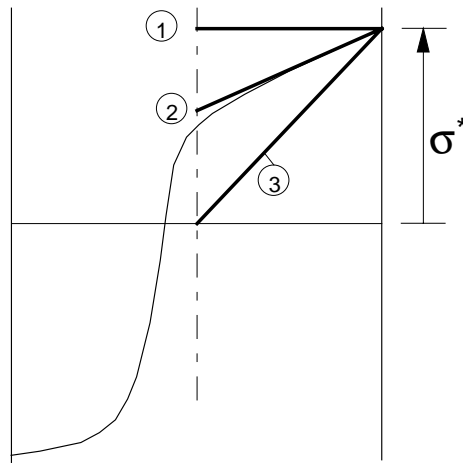


**Fig. 3.2** Approximations of the nonlinear stress distributions by straight lines.

The simple straight-line representations of stresses then read

$$\sigma(y) = \sigma^* \quad \text{for curve (1)} \quad (3.2a)$$

$$\sigma(y) = \bar{\sigma} + (\sigma^* - \bar{\sigma})y \quad \text{for curve (2)} \quad (3.2b)$$

$$\sigma = \sigma^* y \quad \text{for curve (3)}. \quad (3.2c)$$

where  $\bar{\sigma}$  is the stress value at the centre of the bar.

In order to perform numerical computations it is of advantage to express the stress quantities  $\bar{\sigma}$  and  $\sigma^*$  by simple relations. From the curves shown in Fig. 3.3b we find a good agreement between numerically computed stresses (thin curves) with approximations by straight lines (thick lines) for

$$\bar{\sigma} \cong \sigma^*/2$$

providing

$$\sigma(y) = \frac{\sigma^*}{2}(1+y) \quad \text{for curve (2)} \quad (3.2b')$$

From the straight-line approximation illustrated in Fig. 3.3a one can write for the stress range  $40 \text{ MPa} < \sigma_{el} < 80 \text{ MPa}$

$$\frac{\sigma^*}{\sigma_{el}} \cong 0.9 - \frac{0.002}{\text{MPa}} \sigma_{el} \quad (3.3)$$

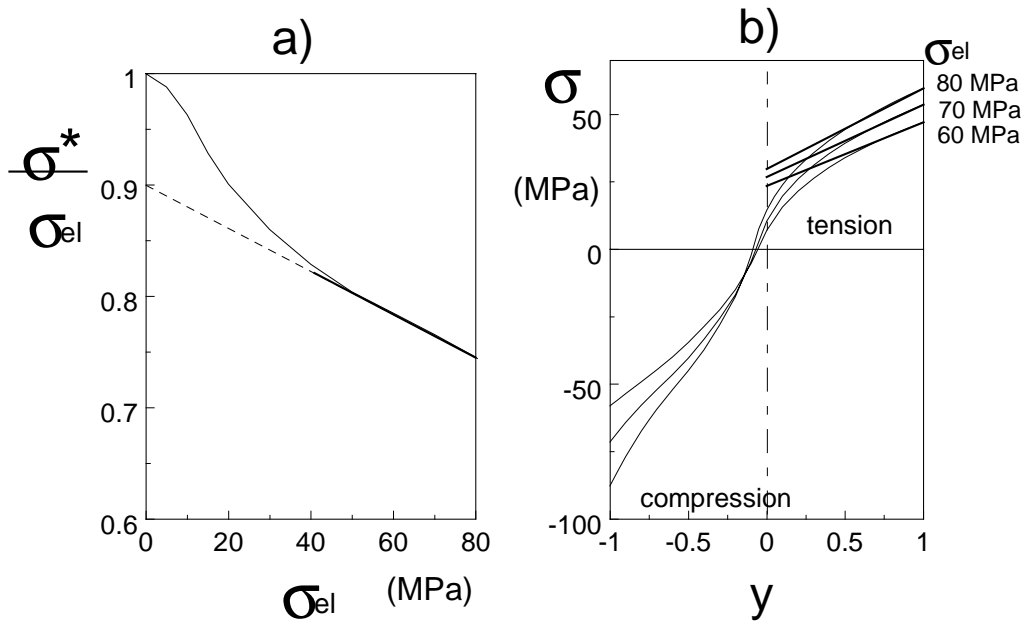


Fig. 3.3 Approximation of the stress state in the tensile region of a bending bar by straight line relations.

### 3.2 Fracture mechanical considerations

A semi-elliptical surface crack is assumed having the initial crack depth  $a_0$  and the initial width  $c_0$ . The applied stress gives rise for the stress intensity factor  $K_{IA}$  at the deepest point and for the stress intensity factor  $K_{IB}$  at the surface points of the crack.

The failure condition in a strength test is given as

$$K_{IA} = K_{IR}(\Delta a) \quad , \quad K_{IB} = K_{IR}(\Delta c) \quad (3.4a)$$

$$\max\left(\frac{\partial(K_{IA} - K_{IR}(\Delta a))}{\partial a}, \frac{\partial(K_{IB} - K_{IR}(\Delta c))}{\partial a}\right) \geq 0 \quad (3.4b)$$

### 3.2.1 Differences in bending and tensile strength in the absence of an R-curve

Since in a bending bar the stress state is different from the homogeneous stress in a tensile specimen the geometric functions  $Y$  for the stress intensity factor solutions are different too. Consequently, different critical stresses result in both cases for a given crack.

First the stress intensity factors have to be determined from crack geometry and stress distribution. If  $Y_t$  is the geometric function for pure tension and  $Y_b$  is the value for pure bending, the stress intensity factors for the three stress approximations can be written

$$K = \sigma * Y\sqrt{a} \quad (3.5)$$

with the geometric functions

$$Y = Y_t \quad \text{for curve (1)} \quad (3.6a)$$

$$Y = \frac{Y_t \bar{\sigma} + (\sigma^* - \bar{\sigma}) Y_b}{\sigma^*} \quad \text{for curve (2)} \quad (3.6b)$$

$$Y \cong \frac{1}{2}(Y_t + Y_b) \quad \text{for curve (2)} \quad (3.6b')$$

$$Y = Y_b \quad \text{for curve (3)} \quad (3.6c)$$

From the failure conditions (3.4a) and (3.4b) the strengths for tension and bending load were determined. They are plotted in Fig. 3.4 for an initial crack size of  $a_0 = 150 \mu\text{m}$  as a function of the initial aspect ratio  $a_0/c_0$ .

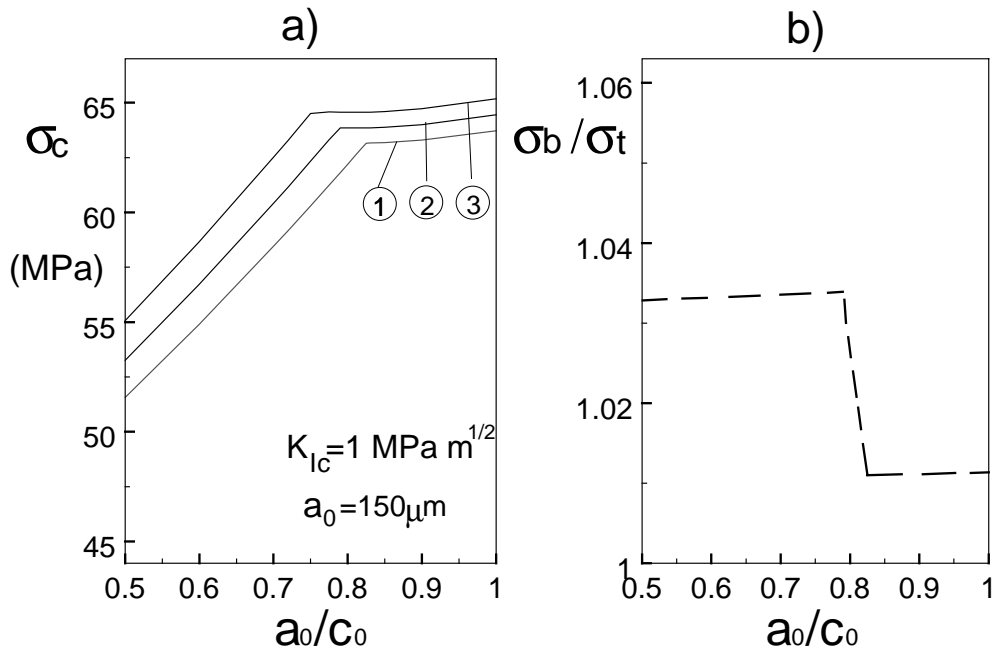


**Fig. 3.4** Strength with R-curve influence: a) bending strength (approximation (2) in Fig. 3.2) and tensile strength for a  $150 \mu\text{m}$  deep crack in dependence of the initial aspect ratio, b) ratio between bending and tensile strengths.

### 3.2.2 Differences in bending and tensile strength including the R-curve

#### 3.2.2.1 Application of an R-curve representation without $K_{I0}$

In order to determine strength in tension and bending, the equations (3.4a) and (3.4b) have to be solved.

If we use the R-curve representation by eq.(2.7), we obtain from eq.(3.4a) a system of two nonlinear equations

$$\begin{aligned} \sigma Y_A(a/c, a/W)\sqrt{a} - A(a - a_0)^m &= 0 \\ \sigma Y_B(a/c, a/W)\sqrt{a} - A(c - c_0)^m &= 0 \end{aligned} \quad (3.7)$$

This system has to be solved for a given stress  $\sigma \leq \sigma_c$  resulting the crack dimensions  $a$  and  $c$ . This can be done numerically using e.g. the Harwell computer subroutine VA02A. Increasing the stress stepwise we have to look for the maximum stress  $\sigma_c$  for which the system remains soluble. If at least for one location (A or B) the condition eq. (3.4b) is violated the computer program cannot find a solution. The related stress value is the strength. For the geometric functions the relations of Newman and Raju [9] for tension and bending were used.

For semi-circular cracks ( $a_0=c_0$ ) and semi-elliptical cracks ( $a_0 = c_0/2$ ) the strength was determined under tensile and under bending loading. The resulting strengths are plotted in Fig. 3.5 for the three stress approximations. As could be expected the highest strength is obtained with the lower limit case (3) and the lowest strength is found with the upper limit stress (1).

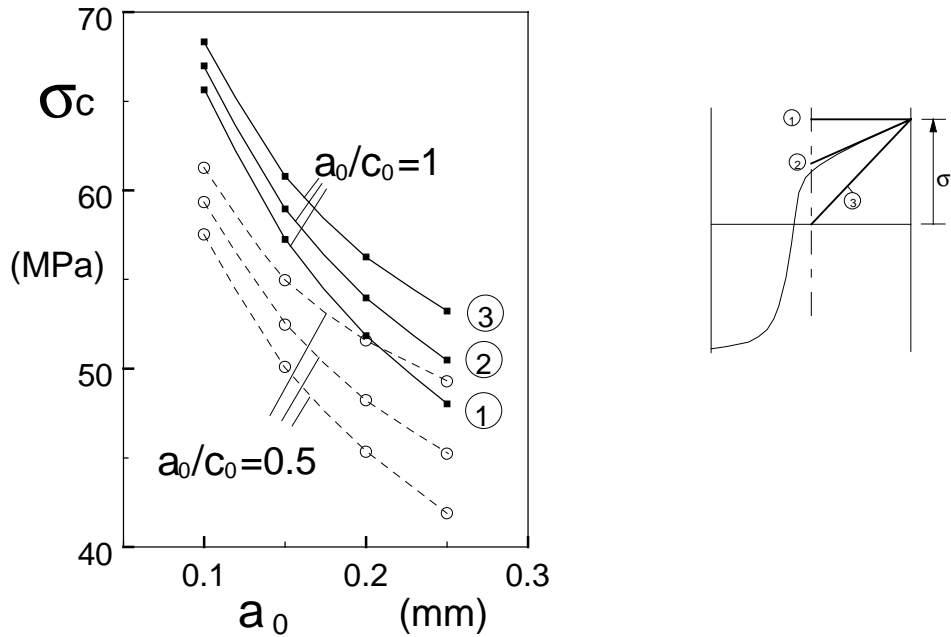


Fig. 3.5 Strength results obtained with eq.(2.7) for the different stress approximations.

The strength results of semi-circular cracks ( $a_0/c_0=1$ ) can be expressed for pure tensile load by

$$\sigma_c=30.0 \text{ MPa } (a_0/\text{mm})^{-0.341} \quad (3.8a)$$

and in a bending test for the best stress approximation (see curve (2) in Fig. 3.5) one obtains

$$\sigma_c=32.85 \text{ MPa } (a_0/\text{mm})^{-0.31} \quad (3.8b)$$

Using the stress distribution shown in Fig. 3.1 we obtain the related elastically computed bending strength, which can be approximated by

$$\sigma_{el,c}=38.5 \text{ MPa } (a_0/\text{mm})^{-0.386} \quad (3.8c)$$

The computations show exponents which significantly deviate from the value  $-1/2$  as has to be expected in the absence of R-curve behaviour. The calculated exponents of eqs.(3.8a) and (3.8c) agree very well with the exponents determined experimentally for the Knoop indentation cracks, which also had an initial aspect ratio of about 1 (see eqs.(2.1a) and (2.1b)).

The development of the aspect ratio  $a/c$  with actual crack depth  $a$  is shown in Fig. 3.6. The aspect ratios tend to a value of about  $a/c \rightarrow 0.8$  (as known also for materials without R-curve). The change in the aspect ratio is "faster" for the bending load than for pure tensile loading. The ratio of the two strength values (bending strength/tensile strength) for a semi-circular crack is plotted in Fig. 3.7 as the solid line for approximation (3) and as the dashed line for the more realistic stress approximation (2). The strengths for two different initial aspect ratios ( $a_0/c_0 = 0.5$  and  $1.0$ ) in approximation (2) are plotted in Fig. 3.8 normalised to the tensile strength (identical with approximation (1)).

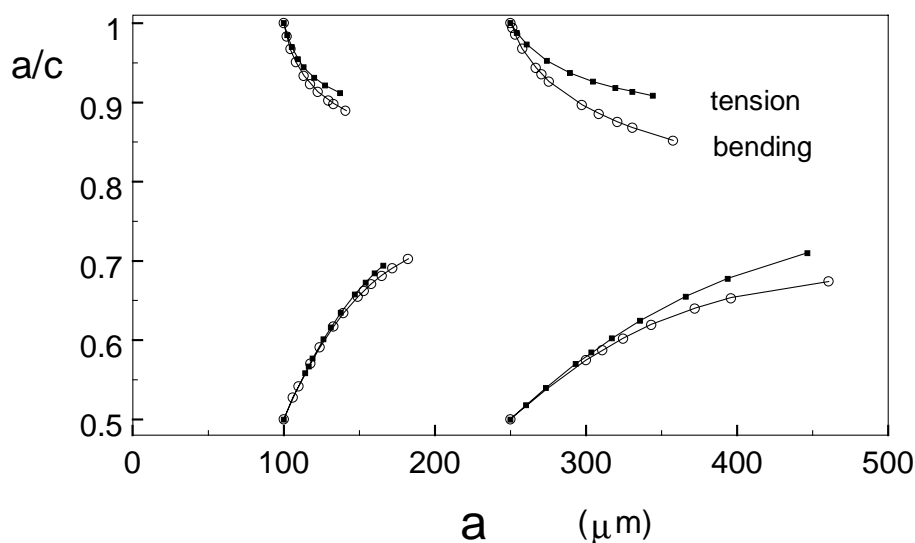


**Fig. 3.6** Change of the aspect ratio  $a/c$  during stable crack propagation until failure.

Figure 3.9a shows the bending and the tensile strength for a crack of initial depth  $a_0= 150 \mu\text{m}$  as a function of the initial aspect ratio. In Fig. 3.9b the ratio of bending strength to tensile strength is represented. Compared with the results for a material in the absence of an R-curve effect (Fig. 3.4) the curves are smoothed by the R-curve.

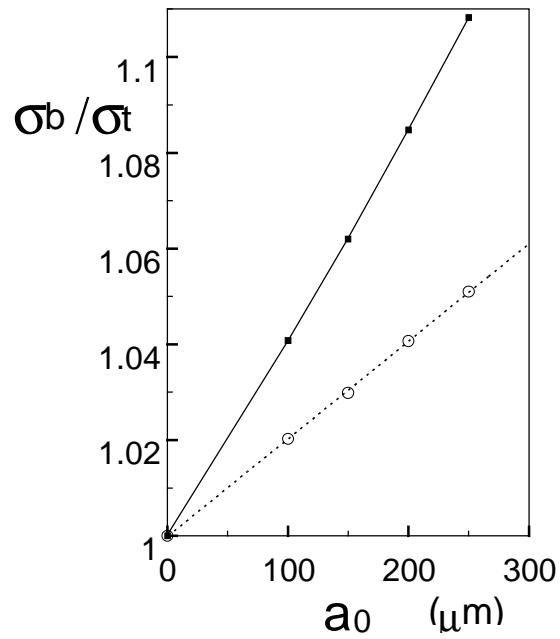


**Fig. 3.7** Ratio between bending ( $\sigma_b$ ) and tensile strength ( $\sigma_t$ ) as a consequence of R-curve behaviour for semi-circular cracks. Bending: solid curve computed with the linear elastic stress distribution (3), dashed curve computed with stress distribution (2) including nonelastic behaviour (see Fig. 3.2b).

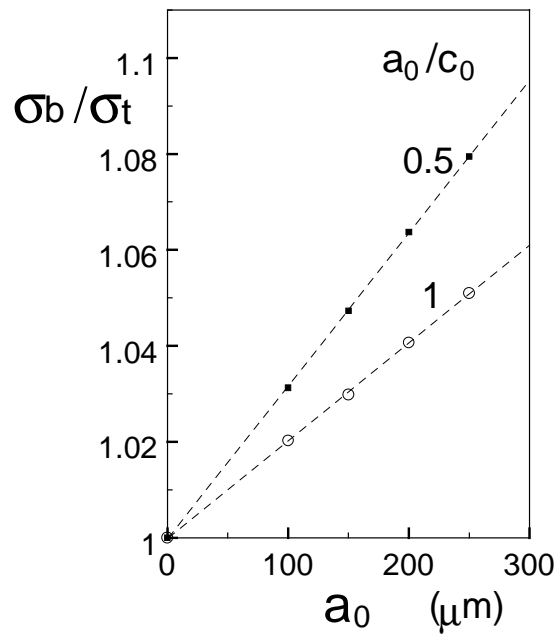


**Fig. 3.8** Ratio of bending strength to tensile strength for cracks with different initial aspect ratio  $a_0/c_0$ . Computations performed with eq.(2.7).

### 3.2.2.2 Application of an R-curve representation including $K_{I0}$

For  $K_{IA}, K_{IB} \geq K_{I0}$ , the evaluation of eq.(2.6) needs the solution of the nonlinear system

$$\begin{aligned} \sigma Y_A(a/c, a/W)\sqrt{a} - A(a - a_0)^m - K_{I0} &= 0 \\ \sigma Y_B(a/c, a/W)\sqrt{a} - A(c - c_0)^m - K_{I0} &= 0 \end{aligned} \quad (3.9)$$

All results obtained with this R-curve description were found to be very close to those obtained without an initial K-value  $K_{I0}$ .

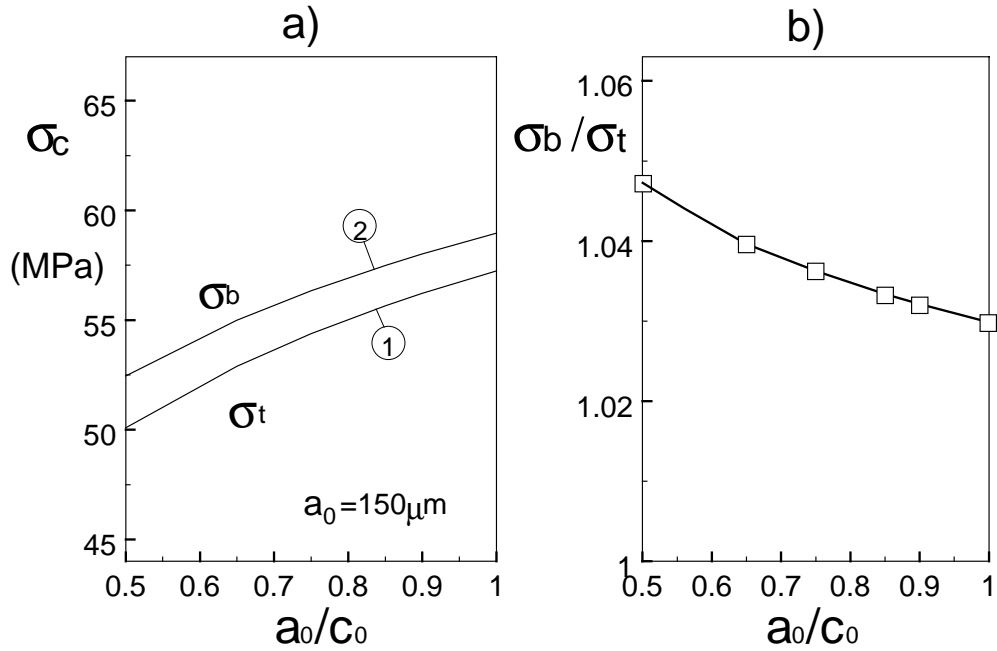


**Fig. 3.9** Strength with R-curve influence: a) bending strength (approximation (2) in Fig. 3.2) and tensile strength for a 150  $\mu\text{m}$  deep crack in dependence of the initial aspect ratio, b) ratio between bending and tensile strengths.

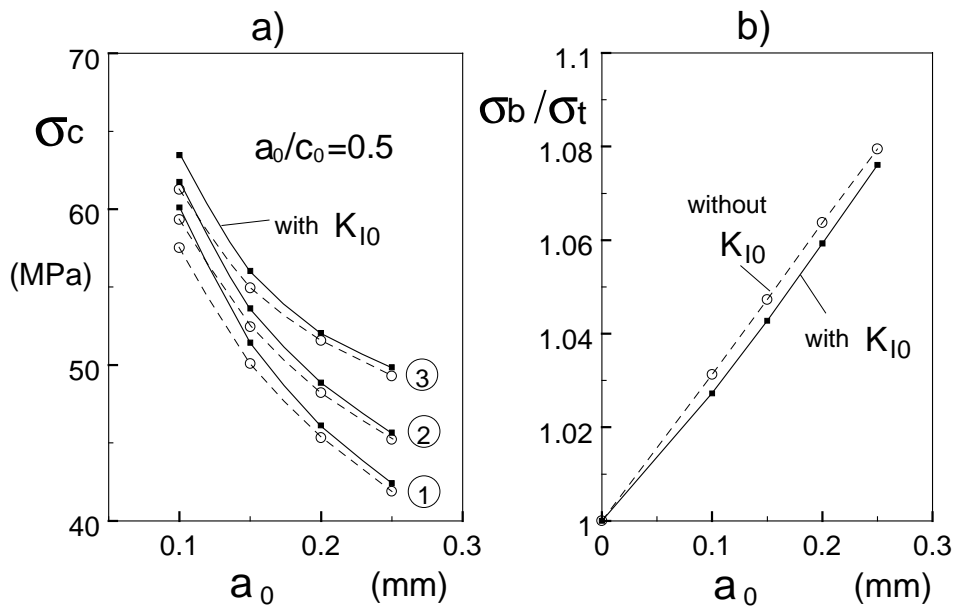


**Fig. 3.10** Comparison between strength data. Solid curves: computed with eq.(2.6), dashed curves: computed with (2.7).



As an example the strengths for cracks with  $a_0/c_0=0.5$  were computed. The dashed curves in Fig. 3.10a were obtained with eq.(2.7), the solid curves with (2.6). Figure 3.10b gives the ratio of the bending strength (approximation (2) used) to the tensile strength (identical with approximation (1) in Fig. 3.2).

### 3.3 Prediction of tensile strength from bending strength results

Tensile strength and bending strength measurements were performed in on unpoled PZT. Figure 3.11 shows the measured tensile strength of PIC 151 as circles. The measured bending strength values are represented as series A (squares). Large differences between the two strength measurements were found.

According to the relation for the failure probability  $F$ ,

$$F = 1 - \exp\left[-\left(\frac{\sigma}{\sigma_0}\right)^m\right] \quad (3.10)$$

the Weibull parameters  $m$  and  $\sigma_0$  were determined with the "Maximum Likelihood Procedure" according to [13] and are given in Table 5. The 90% confidence intervals are represented by the data in brackets.

Test	Parameter m	Strength (MPa)
Tensile strength	11.8 [6.8; 15.8]	$\sigma_{0,t} = 44.5$ [42.3; 46.9]
Bending	15.3 [11.1; 18.9]	$\sigma_{0,b} = 75.3$ [73.5; 77.2]

**Table 5** Weibull parameters for strength tests on unpoled PZT. In brackets: 90% confidence intervals.

The tensile strength data are shown in Fig. 3.11 as the circles and the bending strength results are given by the test series A. Microscopic inspection of the fracture surfaces showed that all specimens failed by surface defects.

In order to allow a direct comparison of bending and tensile strength data, the different surfaces of the specimens (bend specimens with only one side under tensile loading and tensile specimens with four sides exposed to tension) have to be considered. From the strength  $\sigma_{c1}$ , measured with a specimen having the effective surface  $S_{eff1}$ , the strength for a different specimen having the effective surface  $S_{eff2}$  can be predicted by

$$\sigma_{c2} = \left(\frac{S_{eff1}}{S_{eff2}}\right)^{1/m} \sigma_{c1} \quad (3.11)$$

where  $S_{eff}$  is computed by

$$S_{eff} = \int g^m dS \quad (3.12)$$

$$\sigma = \sigma * g \quad (3.13)$$

with the reference stress  $\sigma^*$ , which at fracture is equal to  $\sigma_c$ , and  $g$  is a geometry function describing the stress distribution. In the case of the bending and tensile strength tests it holds simply  $S_{eff1}/S_{eff2}=3.5$  if specimen "1" is the tensile specimen.

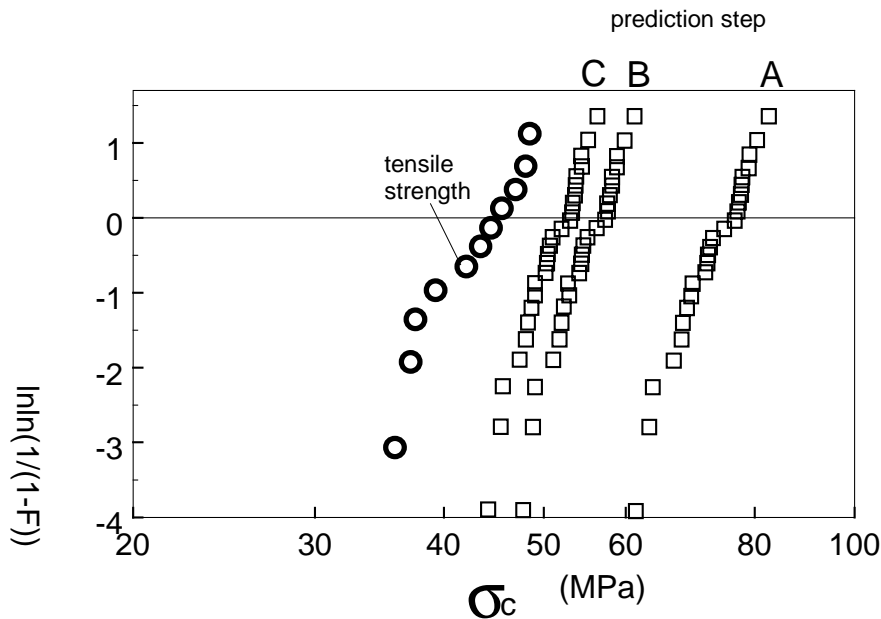


**Fig. 3.11** Prediction of tensile strength from bending strength measurements. A: bending strength measurements; step A $\Rightarrow$ B: elastically computed bending stresses replaced by true outer fibre stress; step B $\Rightarrow$ C: change in strength due to the larger effective surface of the tensile tests as compared to the bending tests. Result C: predicted tensile strength.

In Fig. 3.11 it is illustrated how strong the different single effects and different effective surfaces influence the tensile strength from the bending strength data. In these computations the different effective surfaces of tensile and bending specimens was considered as well as the reduced outer fiber stress in the bending specimens (as a consequence of Fig. 3.1a). Series A in Fig. 3.11 represents the bending strength in terms of the elastically calculated bending strength  $\sigma_{el}$  according to eq.(3.1). The computation illustrated in Fig. 3.11 takes first into consideration the reduced outer fiber bending stress due to the nonlinearity and nonsymmetry of deformation behaviour (prediction step A $\Rightarrow$ B) and the different effective surfaces in tensile and bending tests (prediction step B $\Rightarrow$ C).

Figure 3.12 once more shows the final result of the prediction. A more realistic impression of the confidence situation is given by the combination of the confidence intervals for  $\sigma_0$  and  $m$ . Figure 3.13 illustrates the simultaneous combination of confidence intervals for  $m$  and  $\sigma_0$  according to the Annex of [14]. Only a slight overlapping of the confidence areas is visible.

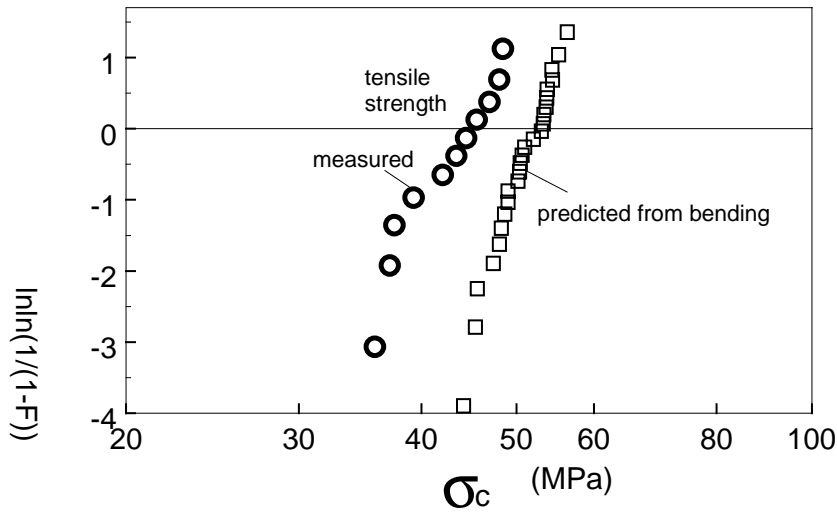


Fig. 3.12 Measured and predicted tensile strength.

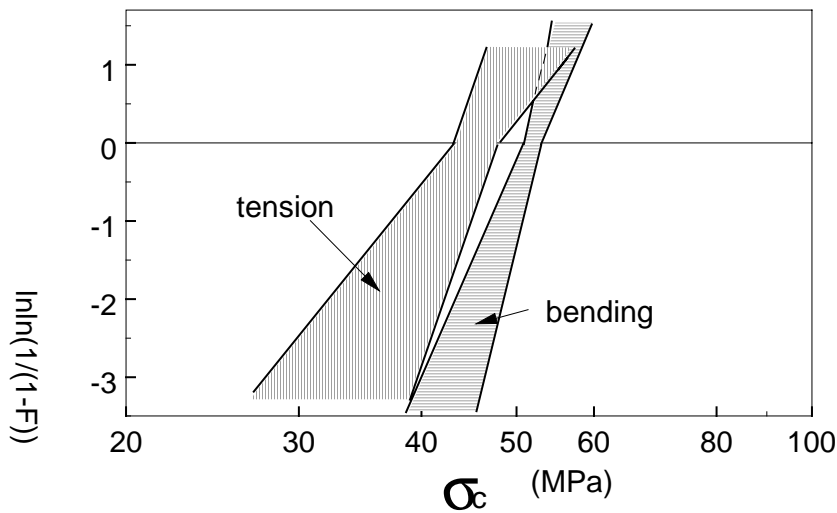


Fig. 3.13 Confidence intervals for the results shown in Fig. 3.9.

In Figs. 3.12 and 3.13 the final prediction and the measured tensile strengths are compared under the simplifying assumptions that:

- the initial crack depth is negligible compared to the specimens size,
- no R-curve is present.

In an improved strength prediction these points have to be included.

In the calculations leading to eqs.(3.8a) and (3.8c) the existence of an R-curve and of a finite crack length were taken into consideration. Combination of eqs.(3.8a) and (3.8c) yields the tensile strength  $\sigma_{t,c}$  as a function of the elastically computed bending strength  $\sigma_{el,c}$

$$\sigma_{t,c} = 30 \text{ MPa} \left( \frac{\sigma_{el,c}}{38.5 \text{ MPa}} \right)^{0.8834} \quad (3.13)$$

In order to show the influence of the single effects the prediction will be considered here step by step starting with the measured bending strength, see data A in Fig. 3.14.

- In the first step A⇒B the actual outer fibre stress at failure is used as the strength.
- In the second step B⇒C again the different effective surfaces are considered.
- The influence of the finite crack size and the R-curve, represented by Fig. 3.5, is considered in the third step C⇒D. Strength distribution D is then the predicted tensile strength.

The Weibull parameters of this final prediction are entered in Table 6. A slight overlapping of the confidence intervals for  $m$  can be detected.

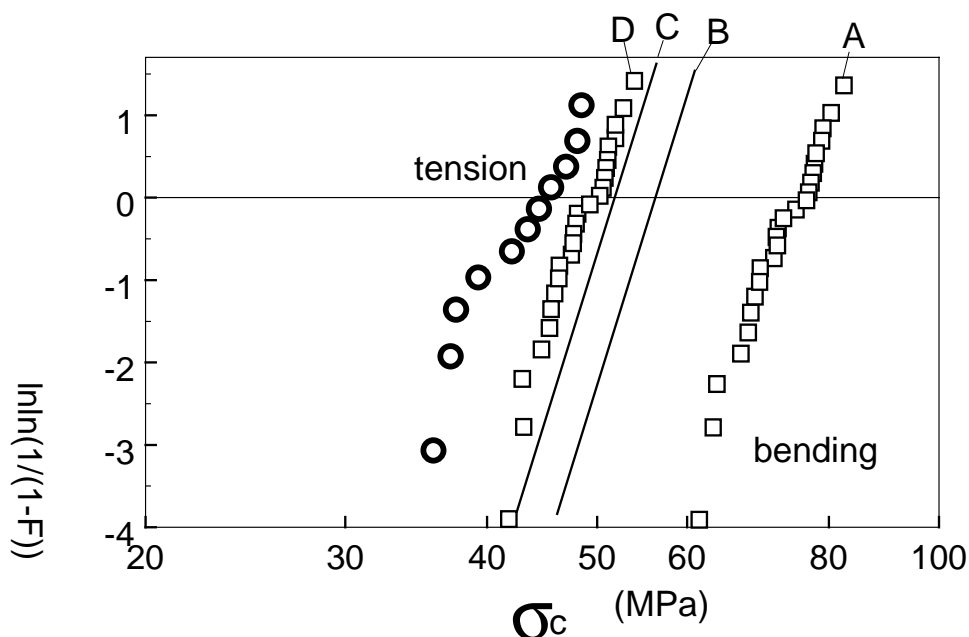


**Fig. 3.14** Prediction of tensile strength from bending strength measurements. A: bending strength measurements; step A⇒B: considering true outer fibre stress; step B⇒C: change in strength due to the different effective surfaces; step C⇒D: influence of finite crack size and R-curve.

Test	Parameter $m$	Strength (MPa)
measurement	11.8 [6.8; 15.8]	$\sigma_{0,t} = 44.5$ [42.3; 46.9]
prediction	17.3 [13.4; 21.4]	$\sigma_{0,b} = 48.9$ [47.8; 50.0]

**Table 6** Weibull parameters of the tensile strength.

In Fig. 3.15 the confidence area for the final prediction is compared with the confidence area of the measured tensile strengths. The overlapping is now more significant than that shown in Fig. 3.13.

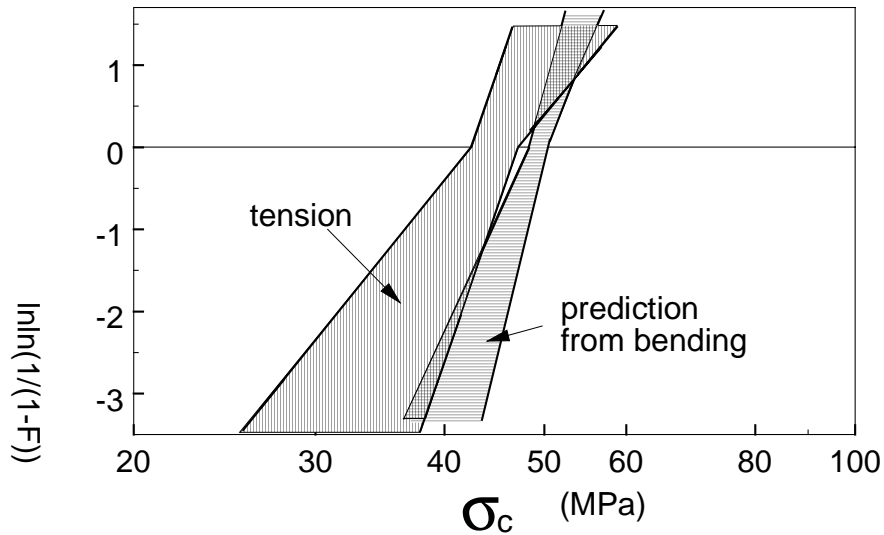


Fig. 3.15 Confidence intervals for the results shown in Fig. 3.14.

### 3.4 Prediction of bending strength from tensile strength measurements

A second possibility of comparison is to predict the bending strength from measured tensile strength data. The procedure is similar to the prediction of tensile strength from bending strength. The only difference is that the prediction is now carried out with the smaller  $m$ -value found for the tensile tests. This leads to a slightly different effect in the influence of the effective surfaces.

The predictions in this direction are shown in Fig. 3.16 neglecting R-curve behaviour and finite crack size and in Fig. 3.17 including these influences.

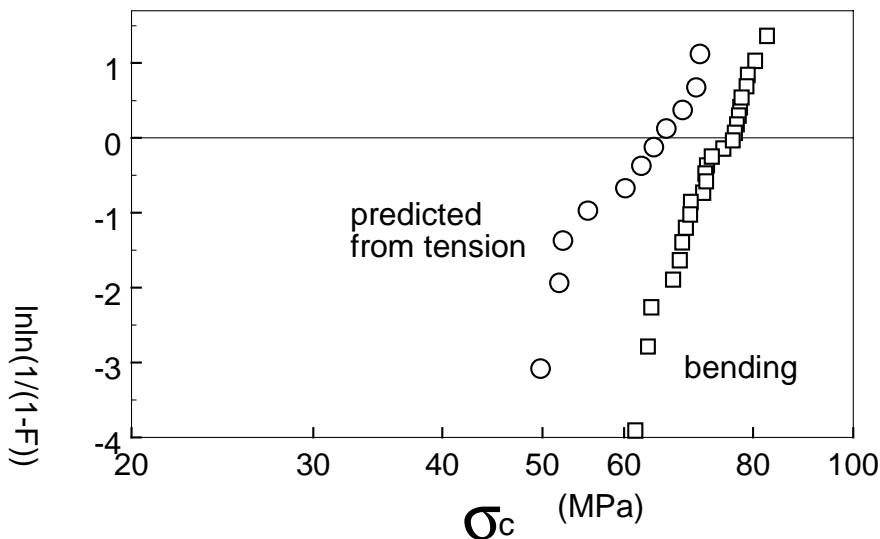
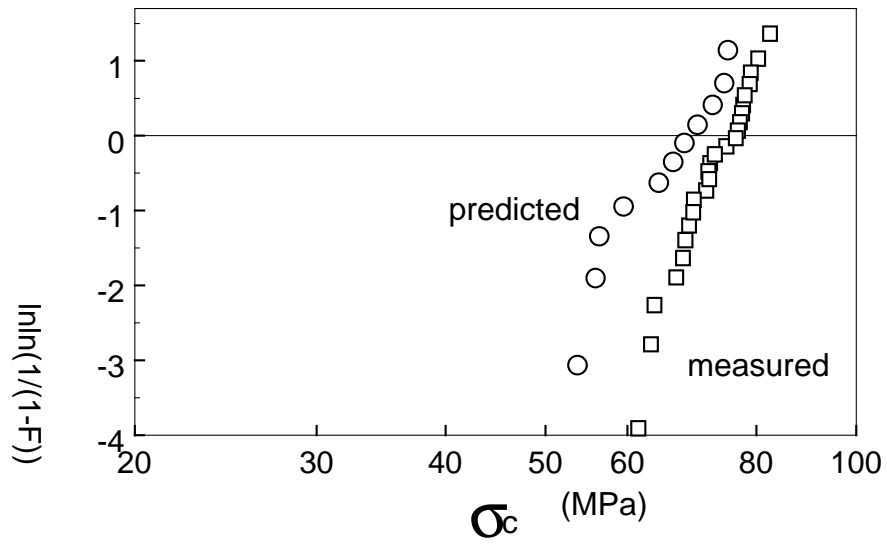


Fig. 3.16 Bending strength predicted from tensile strength measurements compared with measured bending strengths (without R-curve).



**Fig. 3.17** Bending strength predicted from tensile strength measurements compared with measured bending strengths (R-curve and finite crack size included).

## 4 Influence of the R-curve on lifetimes in static tests

Lifetimes in static bending tests are also influenced by R-curve behaviour. In case of a power law for subcritical crack growth the crack growth rates are

$$\frac{da}{dt} = A^* \left( \frac{K_{tip}}{K_{I0}} \right)^n \quad (4.1)$$

where  $A^*$  and  $n$  are material parameters and  $K_{tip}$  is the stress intensity factor governing the stresses at the crack tip. If  $\Delta K_{IR}$  ( $>0$ ) denotes the stress intensity factor caused by the R-curve and  $K_{appl}$  is the externally applied stress intensity factor it holds

$$K_{tip} = K_{appl} - \Delta K_{IR}, \quad \Delta K_{IR} = K_{IR} - K_{I0} \quad (4.2)$$

Equations (4.1) and (4.2) enable to determine the lifetimes in a test under constant load. Numerical computations were performed under the assumption that the R-curve for subcritical crack growth is identical with the R-curve for controlled fracture tests.

Using the R-curve description by eq.(2.6), i.e.

$$\Delta K_{IR} = A(\Delta a)^m, \quad (4.3)$$

we can compute the lifetime numerically. Starting with the initial crack dimensions  $a_0$  and  $c_0$  the applied stress intensity factor is computed for the deepest point and the surface points of the crack from the relations proposed in [9]. During a small time increment  $\Delta t$  the crack extensions  $\Delta a$  and  $\Delta c$  are determined from

$$\Delta a = A^* (K_{tip,A} / K_{I0})^n \Delta t \quad (4.4a)$$

$$\Delta c = A^* (K_{tip,B} / K_{I0})^n \Delta t \quad (4.4a)$$

In the case that the initially applied stress intensity factor is less than  $K_{I0}$  and stable crack extension during load application can be excluded, the crack extension has to be computed according to

$$\Delta a = A^* \left( \frac{K_{appl,A} - A(a - a_0)}{K_{I0}} \right)^n \Delta t \quad (4.4c)$$

$$\Delta c = A^* \left( \frac{K_{appl,B} - A(c - c_0)}{K_{I0}} \right)^n \Delta t \quad (4.4d)$$

If the stress intensity factor at  $t = 0$  exceeds  $K_{I0}$  we have to determine in the first step the amount of stable crack extension at the deepest point and at the surface by solving the system (3.9). If  $\Delta a_s$  and  $\Delta c_s$  denote the contributions of stable extensions, we have to integrate the

same eqs.(4.4c) and (4.4d) but starting now with the initial crack dimensions  $a_i = a_0 + \Delta a_s$  and  $c_i = c_0 + \Delta c_s$ .

A comparison of the strength data for series A of Fig. 3.11 with the bending strength data and the crack sizes for Knoop indentation cracks (Fig. 2.1) shows that the natural cracks in PIC 151 have a mean depth of about 150 $\mu\text{m}$ .

Results of the numerical computations are plotted in Fig. 4.1 for cracks with  $a_0 = 150 \mu\text{m}$ , an initial aspect ratio  $a_0/c_0 = 1$  and different exponents  $n$  of the power law relation eq.(4.1). The curves deviate from straight lines. Nevertheless, the dependencies were fitted within the stress range represented by the dash-dotted box in Fig. 4.1. From the well-known relation between the applied stress  $\sigma_{\text{appl}}$  and the lifetime  $t_f$  (see e.g. [15])

$$t_f = C \sigma_{\text{appl}}^{-n'} \quad (4.5)$$

we obtain the exponent  $n'$  from the slope of the lifetime curve. In the range of straight-line behaviour an apparent crack growth relation between subcritical crack growth and applied stress intensity factor can be derived

$$\frac{da}{dt} = A' \left( \frac{K_{\text{appl}}}{K_{I0}} \right)^{n'} \quad (4.6)$$

with the new parameters  $A'$  and  $n'$  describing the lifetime results sufficiently. The apparent exponents  $n'$  are plotted in Fig. 4.2a versus the correct  $n$ -values. From this result and from the ratio  $n'/n$  plotted in Fig. 4.2b versus  $n$  one can conclude that the R-curve effect leads to apparent crack growth exponents which are about 60% of the correct values for the relation (4.1).

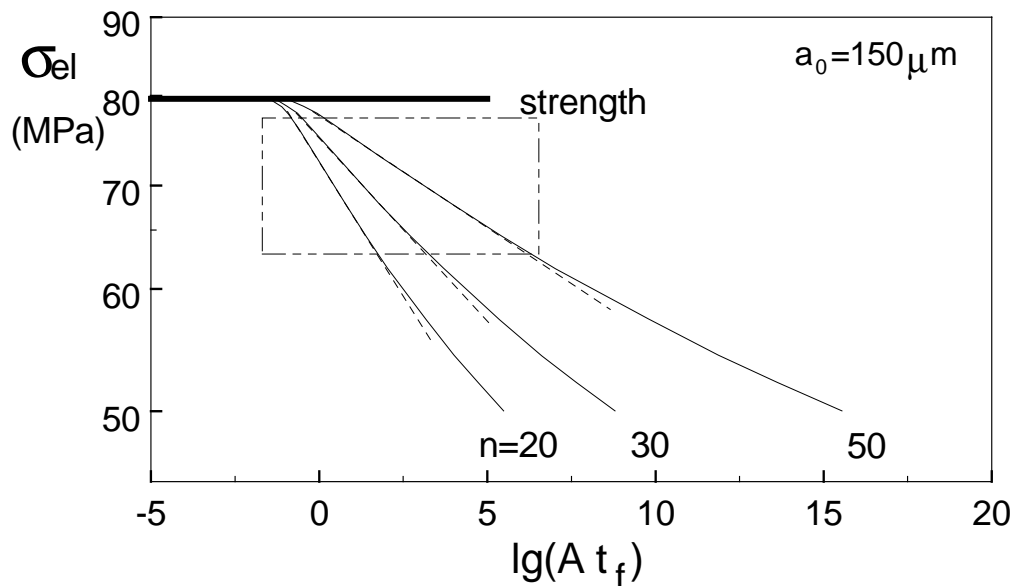


**Fig. 4.1** Lifetime  $t_f$  as a function of the elastically computed bending stress for several crack growth exponents  $n$ .

Dashed lines: straight lines fit for the stress range indicated by the dash-dotted box.



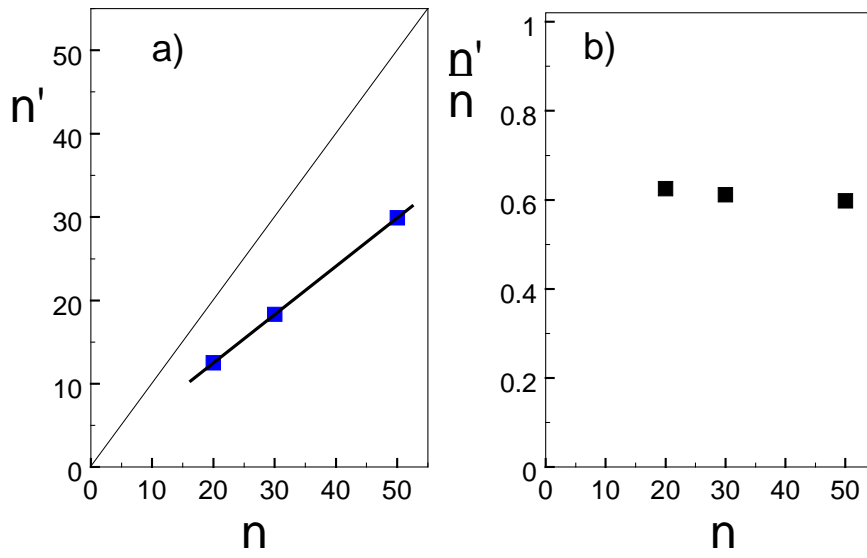


**Fig. 4.2** Apparent crack growth exponent  $n'$  according to the representation eq.(4.6)

## 5 References

- [1] Pohanka, R.C., Freiman, S.W., Okazaki, K., Tashiro, S., Fracture of piezoelectric materials, in: Fracture Mechanics of Ceramics Vol. 5, Plenum Press, New York, 1983, 353-364.
- [2] Freiman, S.W., Chuck, L., Mecholsky, J.J., Shelleman, D.L., Storz, L.J., Fracture mechanism in lead zirconate titanate ceramics, in: Fracture Mechanics of Ceramics Vol. 8, Plenum Press, New York, 1986, 175-185.
- [3] Freiman, S.W., Pohanka, R.C., Review of mechanically related failures of ceramic capacitors and capacitor materials, J. Am. Ceram. Soc. **72**(1989), 2258-2263.
- [4] Meschke, F., Kolleck, A., Schneider, G.A., R-curve behaviour of BaTiO<sub>3</sub> due to stress induced ferroelectric domain switching, J. Europ. Ceram. Soc. **17**(1997), 1143-1149.
- [5] Pferner, R.A., Mechanische Eigenschaften von PZT-Keramiken mit definiertem Gefüge, Thesis University Stuttgart, 1997.
- [6] Rostek, A., Bruchmechanische Untersuchungen an ferroelektrischen Keramiken, Thesis University Stuttgart, 1996.
- [7] Fett, T., Müller, S., Munz, D., Thun, G., Nonsymmetry in deformation behaviour of PZT, J. Mater. Sci. Letters **17**(1998), 261-265..
- [8] Fett, T., Munz, D., Thun, G., Nonsymmetric deformation behaviour of PZT determined in bending tests, J. Am. Ceram. Soc., J. Am. Ceram. Soc. **81**(1998), 269-272.
- [9] Newman, J.C., Raju, I.S., An empirical stress intensity factor equation for the surface crack, Engng. Fract. Mech. **15** (1981), 185-192.
- [10] Nishida, T., Pezzotti, G., Mangialardi, T., Paolini, A.E., Fracture mechanics evaluation of ceramics by stable crack propagation in bend bar specimens, Fracture Mechanics of Ceramics **11**(1996), 107-114.
- [11] Fett, T., An analysis of the three-point bending bar by use of the weight function method, Engng. Fract. Mech. **40**(1991), 683-686.
- [12] Chantikul, P., Anstis, G.R., Lawn, B.R., Marshall, D.B., A critical evaluation of indentation techniques for measuring fracture toughness, II: Strength method, J. Am. Ceram. Soc. **64**(1981), 539-543.
- [13] Thoman, D.R., Bain, L.J., Antle, C.E., Inferences on the parameters of the Weibull distribution, Technometrics **11**(1969), 445.
- [14] European Standard ENV 843-5, Advanced monolithic ceramics - mechanical tests at room temperature - statistical analysis
- [15] Munz, D., Fett, T., Mechanisches Verhalten keramischer Werkstoffe, Springer Verlag, 1989.